The Design of Flexible Organic Photovoltaic Fibers

Rigoberto Antonio Zamora

A thesis

submitted in partial fulfillment of the

requirements for the degree of

Master of Science

University of Washington

2017

Reading Committee:

Christine Luscombe

J. Devin MacKenzie

Program Authorized to Offer Degree:

Materials Science and Engineering

University of Washington

Abstract

The Design of Flexible Organic Photovoltaic Fibers

Rigoberto Antonio Zamora

Chair of the Supervisory Committee:
Associate Professor Christine Luscombe
Materials Science and Engineering

The possibility of using solution processing methods that are vacuum free and low temperatures, are attractive properties of organic π-conjugate polymers. These properties can be used to facilitate the processing of organic electronics such as transistors, organic light emitting diodes, and organic solar cells at lower temperatures. While reducing manufacturing costs remains important, an additional upside to developing organic electronics arises from the innate flexible characteristic of organic polymers. Adding flexibility into the design criteria of electronic devices while simultaneously lowering manufacturing costs, highlights the potential to design solar cells for use in varying applications such as fabrics and textiles. Traditional organic solar cells incorporate planar electrodes into their design. Cylindrical electrodes in the form of wires allow access to novel fabrication methods and enable novel architectures. The wires can be coated with varying hole transporting materials, electron transporting materials, and active layer combinations, just like standard planar electrodes. Ultimately, the wires can be woven together to

form a lightweight fabric to be used in applications where flexibility and functionality is desired. Here we present the design of machinery that enables the fabrication of flexible organic solar cells using a modified dip coating process. The one dimensional in-line coating process can be modified to coat multiple layers at speeds of up to 1.4 m/min using low drying temperatures with a continuous process.

1. Introduction

Forty years after the discovery of doped polyacetylene, a great emphasis is now being placed on developing π-conjugated polymers and small molecule acceptors for electronic devices such as organic transistors, organic light emitting diodes, and organic solar cells.[1] Organic photovoltaics have the potential to enable new applications due their unique properties. While inorganic semiconductors can be designed to behave as flexible devices by decreasing their thicknesses, their weight and high-cost processing methods are unattractive, and limit their applicability when considering large-scale manufacturing costs. An important property of organic semiconductors is the potential to make them solution processable. Solution processing enables the use of lower annealing temperatures to manufacture electronics. Processing methods such as spin coating, dip coating, inkjet printing, and screen printing can be used as scalable fabrication methods that capitalize on the solution processing capability of conjugated polymers, allowing for rapid and low-cost processing of these materials.[2]

The performance of polymer solar cells (PSC) has steadily increased over the last decade. It is critical to understand that a PSC offers a higher coefficient of absorption.[3] The high coefficient of absorption enables a polymeric thin film that is only nanometers thick, to absorb a large amount of the radiation within the thin film's corresponding absorption range.[3] Combining the fact that PSCs have a high coefficient of absorption, lower material cost, and reduced manufacturing expenses, yields the possibility of developing a flexible PSC that can be used in fabrics and textiles. Furthermore, the acme of flexible PSC design and successful integration as textiles or fabrics, arises from the possibility of powering electronic devices when a traditional power source is not available.

2. Background

At the heart of any organic PSC is the active layer. Initial active layer configurations consisted of two separate layers that contained a planar junction. One of these layers is made of a π-conjugated polymer and acts as the electron donor. Conversely, the other layer is an acceptor and could be either a π-conjugated polymer or a small molecule. The active layer is responsible for generating an exciton, and leads to the creation of an electron-hole pair after excitation from the highest occupied molecular orbital (HOMO) of the donor polymer to the lowest unoccupied molecular orbital (LUMO).

A planar heterojunction active layer requires that the electron and holes travel through separate layers before reaching their corresponding electrodes. If a separated electron generated in the donor layer, traversed through the acceptor layer and found an unpaired hole, they would recombine and effectively reduce the efficiency of the PSC. Efforts to reduce the distance an electron and hole would travel before reaching the electrode, lead to the discovery of the bulk heterojunction (BHJ).[4] By blending the donor and acceptor materials together with average thicknesses of each domain being on the order of the exciton diffusion length, the BHJ has proven to produce some of the highest power conversion efficiencies with the addition of electron and hole transport layers.

A traditional PSC makes use of a combination of layers that enable hole and electron extraction to occur while minimizing recombination, thereby increasing the overall performance of the PSC. Furthermore, correctly selecting materials for these layers can increase the overall stability of the PSC. Conventional PSC architecture makes use of a transparent conduct oxide (TCO) that is considered the anode electrode, where additional layers that include the hole transport layer (HTL), the BHJ active layer, the electron transport

layer (ETL), and the cathode are deposited sequentially. A conventional PSC architecture is depicted in **Fig. 1a**. An inverted PSC follows a similar design to the conventional PSC, with the exception that stacking order of the ETL and HTL have been switched. This is depicted in **Fig. 1b**, where the ETL is deposited on the cathode and the corresponding BHJ, HTL, and the anode is deposited after. Inverted PSCs have been reported with improved stability and currently hold the highest power conversion efficiency (PCE) for a single heterojunction design.[5] The PCE of a PSC is a ratio of the output electric power to the solar incident power.

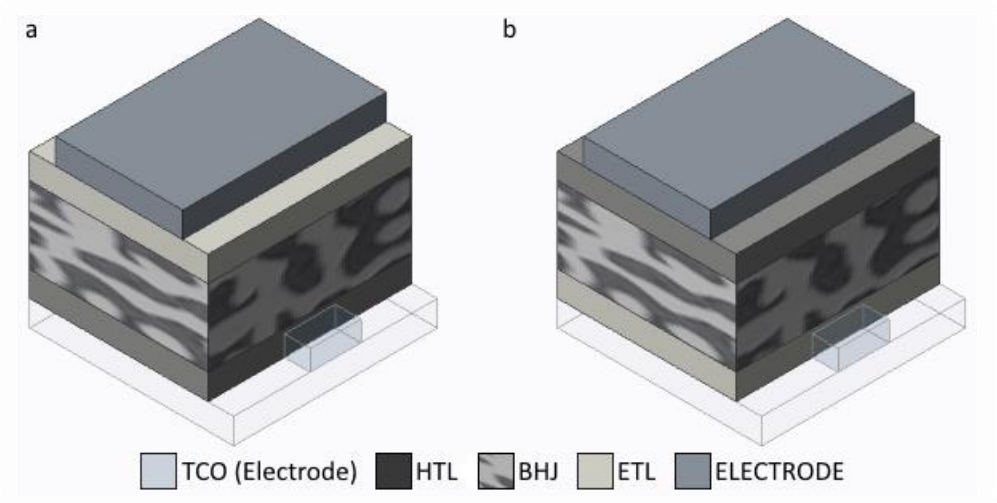

Figure 1. (a) Device architecture of a conventional BHJ PSC and (b) an inverted PSC.

The effects of each layer in a PSC has been a topic that has been studied significantly.[6,7] The stability of the layers that are being processed effect the overall performance of the PSC. Features such as surface morphology, interface interaction, and vertical/ lateral phase separation of the previous layer are functions of solvent selection, annealing temperature, and donor/acceptor ratio.[6] Donor polymer poly(3-hexylthiophene) (P3HT) and fullerene acceptor [6,6]-Phenyl C_{61} butyric acid methyl ester (PCBM) have been commonly utilized in the design of PSCs. Of significant importance is preventing aggregation in the active layer components,

as this can reduce the ability of the device to separate an exciton, and to extract electrons and holes. The addition of a thermal annealing step has been shown to improve the crystallinity of P3HT while the use of solvent additives has improved the morphology of the BHJ.[7]

Metal oxides have been used as the electron transport layer (ETL) in organic PSC due to their ability to facilitate transportation of electrons to the cathode.[8,9] They also function as effective hole blocking materials due to their offset valence band energy level with the acceptor polymer. Furthermore, the metal oxide thin films can have a significant effect on the series resistance of the device. A thicker metal oxide layer will increase the series resistance of the device, decreasing the overall performance of the PSC. It has been reported that metal oxides such TiO_x as can increase the air-stability of the PSC. Where the TiO_x acts as a barrier to humidity and oxygen, a feature that arises from the oxygen deficiency in the material.[9] Some other low work function transition metal oxides include ZnO and ZrO_2. An additional parameter when selecting an ETL for a PSC is the ability to create a solution processable precursor that is compatible with the other deposited layers.[10]

The hole transport layer (HTL) is integrated into the design of a PSC to facilitate the transportation of holes to the anode.[8,9,10] As a counterpart to the function of the ETL, the HTL is an effective electron blocking material. A widely utilized organic HTL is poly(3,4-ethylenedioxithiophene):poly(styrene sulfonic acid) (PEDOT:PSS). PEDOT:PSS features a high work function and forms an ohmic contact with most donor polymers.[9] However, PEDOT:PSS performance suffers in the presence of water, is acidic, and in large scale

manufacturing, duplicating morphology has been proven difficult.[9] Metal oxides such as V_2O_5, MoO_3, and Cu_2O have also found a use as HTL in conventional and inverted PSCs.

With a general understanding of the independent layers of a PSC design, the focus can now shift towards highlighting some of the high capacity, scalable methods of fabricating PSCs. Considered third-generation solar cells, PSC advantages are largely attributed to lower weights, the solution processing capability of thin films, and the potential to be used in applications that require flexible materials.[8,11] These advantages have permitted novel PSC designs of flexible textiles and fabrics that are based on fiber electrodes.

2.1. Roll-to-Roll Printing

Conventional roll-to-roll (R2R) methods of preparing thin film organic electronics have been largely attractive due to the potential of developing devices at fast rates while implementing low cost processing methods. The desired speeds of R2R coating and printing techniques falls within a minimum criterion of 1-20 m/min, with speeds of 60-300 m/min being preferable.[12] While many publications iterate that implementation of a lab developed electronic devices can easily be scaled up, it remains a challenge to replicate the efficiency and performance of devices fabricated in a controlled lab environment. With that in mind, several R2R methods will be discussed that are considered the most prominent thin film disposition methods.

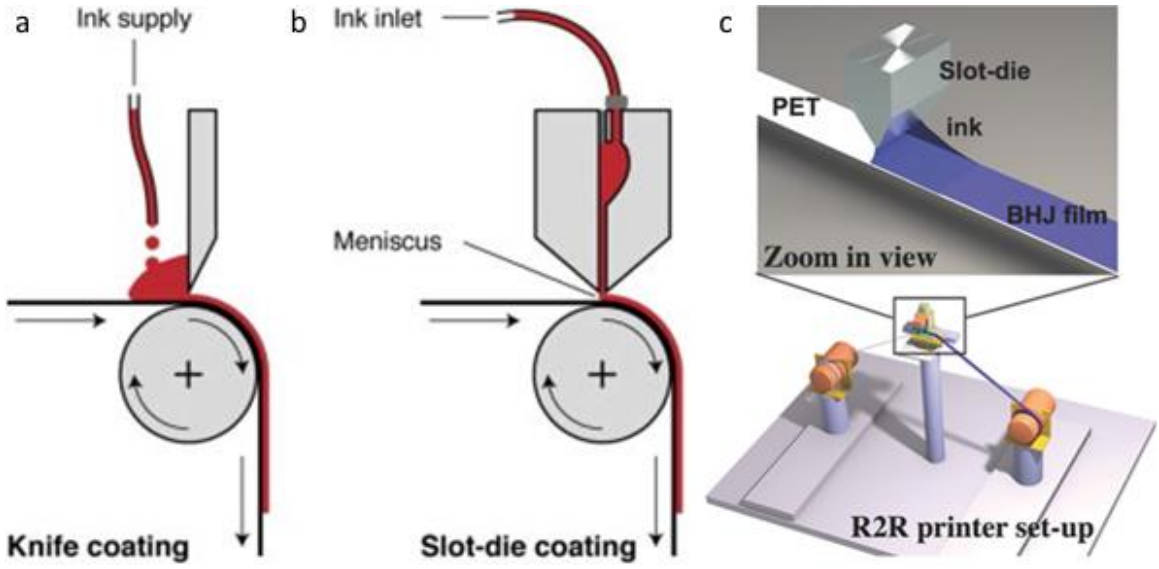

Figure 2. (a) Illustration a knife coating setup, (b) a slot-die coating setup, and (c) a complete R2R slot-die schematic. Reproduced with permission from [12,13].

2.1.1. One Dimensional R2R Coating Processes

In knife coating, a substrate is pulled through a finely tuned gap. Ink is deposited in front of the knife and as the substrate is pulled through, only the amount of ink that can pass below the knife is permitted through. The final coat thickness can be estimated to be half of the gap height.[12] Knife coating is considered a one dimensional R2R process, where the final coat is not intended to be patterned or molded (**Fig 2a**). The slot-die coating process depicted in Fig. 2b, features a similar design to knife coating with the exception that the ink is deposited via an orifice within the die. The thickness of the deposited layer is fully dependent on pump speed, width of the meniscus, and web speed. Both coating techniques can utilize viscous inks and solvents. Processing speeds can be performed at 0.1-200 m/min, where organic solar cells have successfully been manufactured at 5 m/min. In coating processes, surface tension and surface energy are factors that can be overlooked. As opposed to printing processes, where they become important variables that determine whether the ink is successfully transferred.

2.1.2. Two Dimensional R2R Printing Processes

Contrary to coating processes, printing processes allow predefined film patterns to be developed. Printing processes are therefore considered two dimensional R2R processing methods. Fully continuous processes such as gravure printing (**Fig. 3a**) and flexographic printing (Fig. 3b) feature printing speeds of up to 900 m/min.[12] In gravure printing, a gravure cylinder with surface features, cut as cavities into the surface of a drum, is used to imprint a patterned layer onto a substrate. The cavities must be continuously refilled in an ink bath, where a doctor blade removes any excess ink. A softer impression cylinder is used to ensure that good contact is made between the gravure cylinder and the substrate. The process is largely dependent on the surface tension transfer of ink and is more suitable for printing of low viscosity inks.

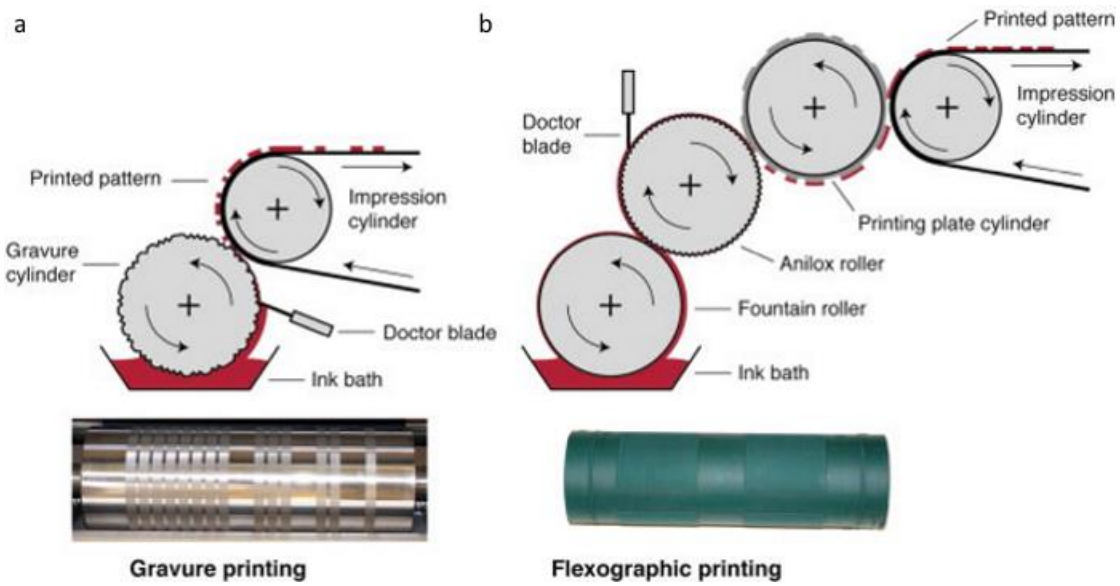

Figure 3 . (a) Illustration of gravure priting and (b) flexographic printing. Gravure printing can be used to coat layers on subtrates at speeds of up to 15 m/s. Reproduced with permission from [12]

In flexographic printing (Fig. 3b), a printing plate cylinder, which acts as a traditional stamp, is used to transfer the ink to the substrate. To ensure that ink is always coated on the

printing plate cylinder, a ceramic anilox cylinder is used with microcavities on the surface. Excess ink on the anilox cylinder is removed by a doctor blade. The ink on the anilox cylinder is provided by the fountain roller. Other processes that can be used include screen printing, inkjet printing, and spray coating.

It remains to be stated that certain R2R processes are better suited coating for different layers. Issues that still need to be resolved to improve the performance of R2R processes are based on improving the registration. Improved registration will facilitate the alignment of different layers and permits processing at higher speeds. A key note being the necessity to develop in-line processes that enable the coating of different layers on the same run and at lower drying temperatures.

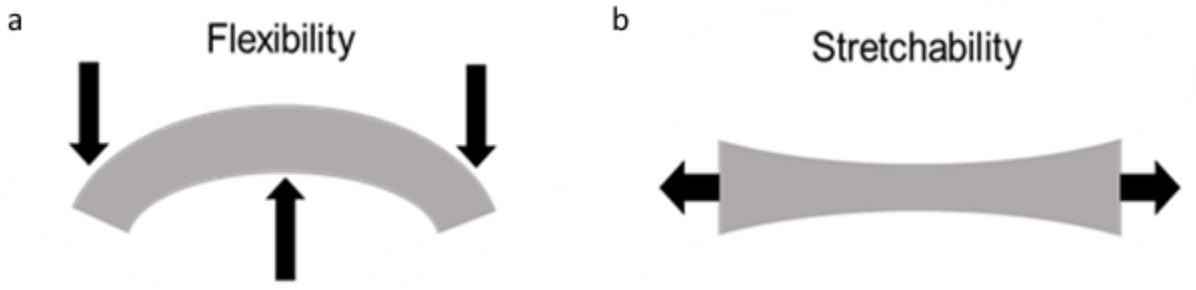

Figure 4. (a) Establishing the difference between flexible and (b) stretchable electronics. Reproduced with permission from [11].

2.1.3. Flexibility and Strechability in Organic Electronics

It is important to distinguish the difference between an electronic device that is intended to be used in a flexible application from a stretchable application. Through a mechanical perspective, the electronic device will have a moment response to outside forces that are being applied. This is depicted in **Fig. 4a**, where the electronic device experiences flexion. Furthermore, in flexible electronic devices that make use of a fibril electrode, it can be noted that one side of the fiber will experience tension and the other side will experience

compression. If the fiber has been coated with multiple layers of semiconducting polymers, the interface between each layer of the fibril becomes a crucial factor to consider. For stretchable electronics devices, the device is intended to be pulled in a manner that would mechanically resemble a two-force member (Fig. 4b).

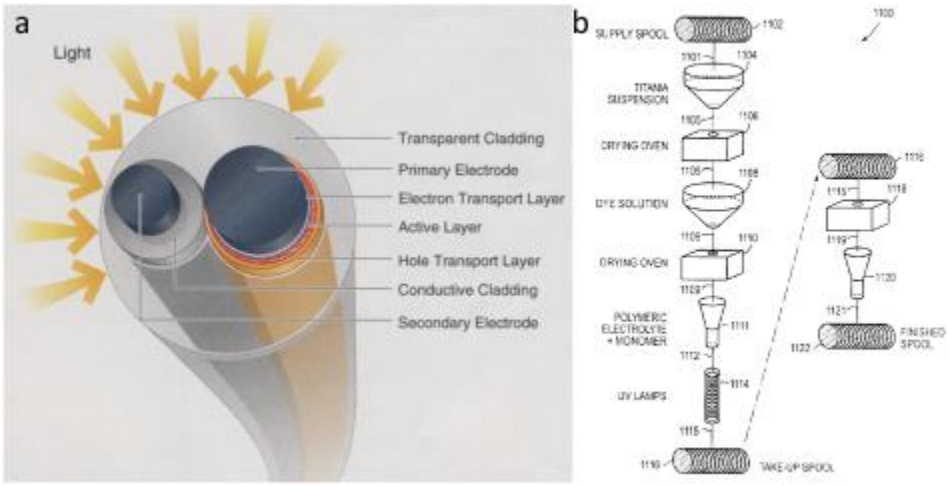

Figure 5. (a) Fiber based PSC that was fabricated by Konarka Technologies in the late 2000's featuring SS wire electrodes. (b) Cup coating process as explained in U.S. Patent No. US 6,913,713 B2. Reproduced with permission from [14].

3. Motivation

In 2009, Konarka Technologies published an article which detailed the fabrication of one of the first commercially available flexible solar wires.[14] An example of the PSC that was manufactured is depicted in **Fig. 5a.** The design featured the use of a 101.6 μm stainless steel (SS) wire electrode and a 50 μm SS secondary electrode. If the surface of the wire was smooth enough and the manufacturing processes ensured that no large surface features were present, the possibility of shorting between the electrodes could be eliminated. Considering that organic solar cells feature thin photoactive films that are in the nanometer range, large variances in the electrode surface features would have decrease the PCE. Furthermore, the use of a cylindrical electrode ensured that the electrons generated in the active layer would only need to travel 100

nm before reaching the primary electrode. If the wires were wound around one another, the holes would only need to travel a maximum of 157 μm to reach the secondary electrode.

To coat the SS wires with their respective layers, a series of vertically positioned cup coaters were utilized (Fig. 5b, 1104, 1108, 1111, and 1120). Each cup coater had a finely cut orifice on the bottom surface that what would enable the fine wire to be drawn through and coated. The 101.6 μm primary electrode was initially coated with an isopropanol solution of titanium butoxide, which was annealed between 90 °C – 100 °C to produce an amorphous layer of TiO_x . The active layer, which consisted of 1:0.8 weight ratio of P3HT to PCBM, was coated onto the wire and annealed at 120 °C. The final layer on the primary electrode was the hole transport layer and consisted of PEDOT: PSS. A separate 50.8 μm SS electrode was then coated with silver paste to increase the conductivity of the wire. To ensure a compromise between charge collection and light transmission, the coated secondary electrode was wound around the primary electrode at a predetermined spacing interval of 1.25 cm per rotation. As the wire is wound around the primary electrode, the secondary electrode is kept under tension to ensure that contact between the two surfaces. The wires are then covered in epoxide and enter an ultraviolet irradiation chamber, which hardens the cladding. The PCE of the fiber was dependent on the orientation of the solar wire in relation to the light source and varied from 2.79% to 3.27%.

Since the initial publication of Konarka Technologies PSC, many novel designs have been presented that highlight the use of different electrodes. The architecture of PSC fibers is based on designs that features a core-sheath fiber electrode or twisting dual fiber electrodes.[15] Attempts have been made at coating cotton fabrics with conducting materials or integrating conducting electrodes among the textile fibers.[16] Flexible PSC designs where a titanium

primary electrode is used in lieu of SS have been published. When compared to 316 SS, unalloyed pure titanium features a lower work function than SS (4.33 eV), a lower electric resistivity ($0.52\ \mu\Omega\cdot\mathrm{m}$), and lower density ($4.51\ \mathrm{kg}\cdot\mathrm{m}^{-3}$). The primary reasons that Konarka was unwilling to use titanium electrodes were due to increased surface features from the manufacturing process, the availability, and cost. Despite the risk, Zhang et al. included an electrochemical anodization step to induce growth of TiO_2 nanotubes before the titanium wire was coated with TiO_2 nanoparticles.[17] This permitted the fabrication of the PSC that is depicted in **Fig. 6a**. The PSC features a counter electrode that is based on multiwall carbon nanotube fibers. The highest achievable PCE for the PSC was 1.78% and after 1000 cycles of fatigue testing the PCE decreased by 15%.

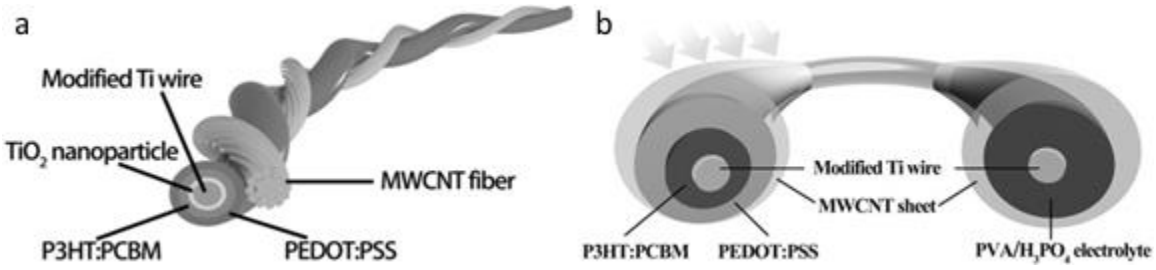

Figure 6. (a) Wire shaped PSC with Titanium electrode wire and (b) an energy storage device has been added to the end of the PSC. Reproduced with permission from [17, 18].

Flexible PSC designs that were previously not feasible due to limitations on the production of large rolls of graphene, can now be implemented into large scale flexible PSC.[19] Using R2R processing methods, 100 m rolls of graphene have been manufactured using Cu foils which are heated in H_2 and methane.[20] The graphene that is produced from the process, can then be transferred onto PET substrate for use in flexible devices such as touchscreens or PSC. The graphene encapsulated PSC is based on a core sheath architecture and achieved a PCE of

2.53% under ambient light with a maximum of 4.36% when combined with a reflector. An example of a graphene encapsulated PSC is depicted in **Fig. 7**.

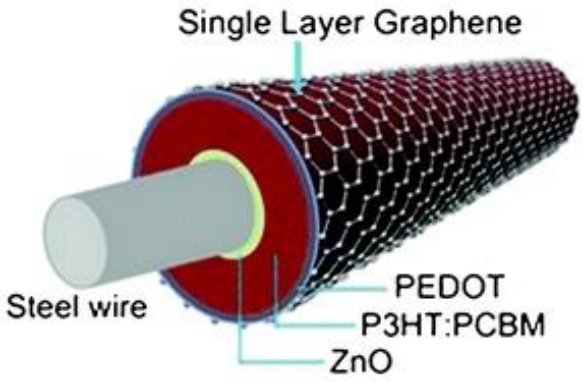

Figure 7. Graphene encapsulated PSC. Reproduced with permission from [19].

With a general understanding to model a flexible solar fiber design, the focus of this article will be on the design of machinery that facilitates production of PSC fibers. The machinery that was designed features a one dimensional continuous in-line coating process using annealing temperatures under 150 °C. An in-depth review of the parts that were designed will be discussed, followed by a general review of the software to operate the machinery, an analysis of the first successfully coated layer and a discussion of modifications that can be made to improve the overall performance of the machinery.

4. Methods

The design process of creating a mechanism that would permit the fabrication of a PSC, evolved around multiple criteria. (1) The machine assembly needed to fit inside a fume hood for safe handling of the solutions. (2) The machine design needed to be modular. (3) Linear control of position was needed along the x-axis of the mechanism. Furthermore, a rotational axis was necessary along the x-axis. (4) A mechanism that finely controlled tension needed to be designed or purchased. (5) An oven was needed to anneal or dry the corresponding layers.

The oven needed to remain under steady state operation. (6) A process and method to coat the fiber needed to be selected. Implementation of the coating technique required the design of a mechanism. (6) The design of fixtures that permitted modifications in the x, y, and z planes would facilitate placement of all the mechanisms that were discussed.

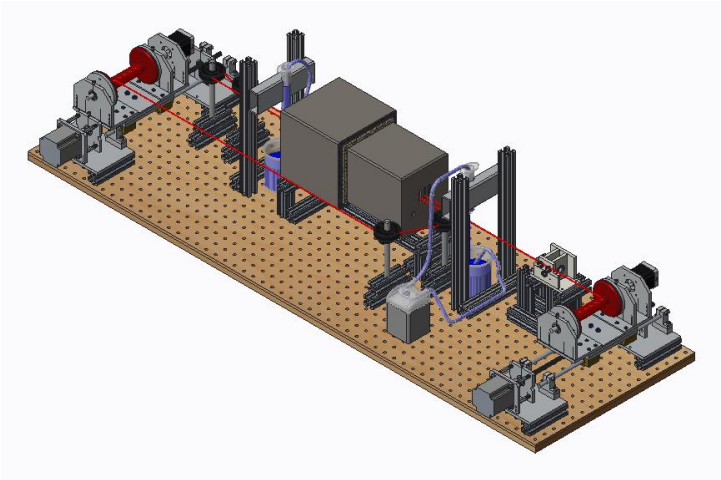

Figure 8. 3D Rendering of the machinery that was designed to coat the SS wire electrodes. Motor 0 and 1 (M0 and M1) are shown in grey. Motor 3 (M3) is shown on the left in black and Motor 2 (M2) on the right is also depicted in black.

4.1. Order of Operations

The following procedure was used in the coating process of the SS wire. The wire was wound onto a spool attached to Motor 2 (M2) of the carriage assembly depicted on the right of **Fig. 8**. The wire was guided around the three-pulley tension sensor. The wire was guided through the oven with a 48 cm long double pointed needle. The wire was fixed onto the spool attached to Motor 3 of the carriage assembly depicted on the left of Fig. 8. The plunger on a syringe was removed and a syringe pump was used to circulate fluid between a beaker and the syringe. After the pump was turned on, the amount of solution within the barrel was allowed to reach steady state. The location of the syringe needle hub was adjusted to permit solution to free-fall onto the wire. A preload was applied on the wire by activating the spool on M3 and

setting the speed of M2 to zero. Motors speeds of 1, 3, and 10 revolutions per minute (RPM) were used to generate samples which contained different coat thicknesses. As the wire progressed under the syringe coater, an oven dried the wire at 120 °C for 156 s (1 RPM), 52 s (2 RPM), and 15.6 s (10 RPM). The amount of time spent in the annealing oven could be adjusted by varying the length of the two-piece oven. To coat multiple layers on the same run, a pulley could be added after the wire was annealed to route the wire back 180°, and an additional syringe coater could be integrated into the coating process.

4.2. Characterization Equipment

Characterization by Atomic Force Microscopy (AFM) was completed by using a Bruker ICON. Scanning Electron Microscopy (SEM) and Energy Dispersive X-ray Spectroscopy (EDS) was completed using a JOEL JSM-6010PLUS/ LA. Profilometry was completed using a KLA Tencor Alpha-Step 500.

5. Results

The overall design of the mechanism that was assembled to facilitate the fabrication of the solar fibers is depicted in Fig. 8. To allow the coating machinery to be operated in a fume hood, a base was designed out ¼" thick plywood with and array of ¼" holes spaced at 1" intervals. The t-slots allowed mounting to the intervals between holes and permitted quick modification to the general layout of the assembly.

5.1. Oven Design

An oven was designed and fabricated using 1/8" 4130 steel sheets (McMaster-Carr), four 150 W cartridge heaters (McMaster-Carr), a 120 VAC solid state relay (Digi-Key), four shaft collars (McMaster-Carr), high temperature chemically resistant rope edge seals (McMaster-Carr), and highly refractive cement. A MYPIN TA4 was used as the proportional-integral-

derivative (PID) controller for the cartridge heaters. The oven was designed to permit the sections to slide between each other. The oven can be shortened to 15.9 cm and extended to 31.1 cm. Additional sections can be added to increase the annealing time. Multiple threaded rods and stepper motors can be added that permit adjustment of the oven as a function of M2 and M3 speeds. By varying the length of the oven, the annealing time can be held constant at different motor speeds. The final oven design is depicted in **Fig. 9**.

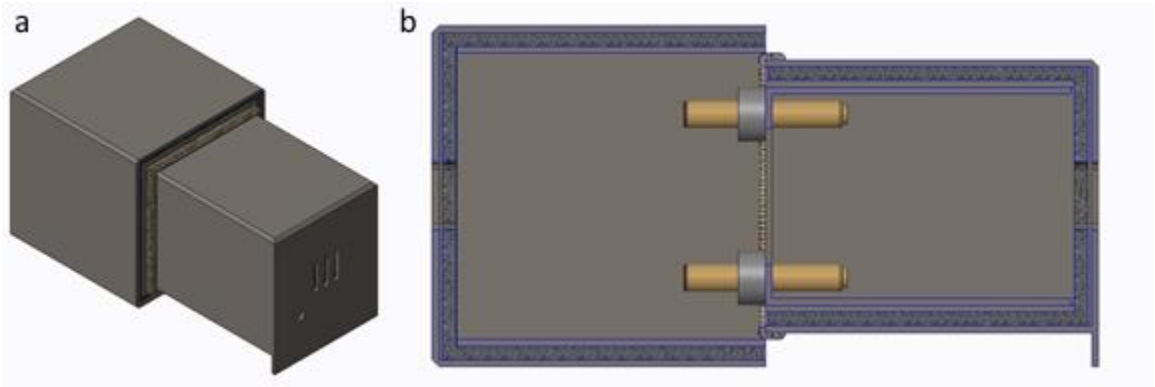

Figure 9. (a) Isometric view of the oven that was designed and fabricated out of 4130 steel sheets and (b) a section veiw of the oven clearly depicting the location of the heat cartidges.

5.2. Coater

For small scale applications, a syringe containing a precursor solution can be used with a collecting beaker placed directly under the syringe. The solution can then be coated along the fiber, collected in the beaker, and recirculated using a pump to the syringe. If the pump is set to circulate fluid into the syringe at the same rate that the syringe is dropping liquid, the system can be determined to be at steady state. This permits the syringe coating method to be modeled as a modified dip coating process. In which case, the Landau-Levich equation can be used to determine the thickness of the coating being applied. As the quantity of wire that needs to be

coated increases, the syringe coater can be replaced with a dip coating bath. The syringe coater that was designed and fabricated is depicted in **Fig. 10**

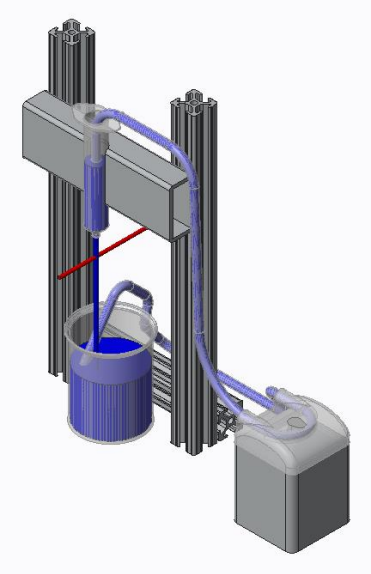

Figure 10. Isometric view of the syringe coater with a Baron Grey Beard pump coating a fiber. The pump circulates the solution from the beaker to the syringe. When the solution in the syringe reaches steady state, the coating process is initiated.

5.3. Linear Actuator with Lead Screw

To facilitate the spooling of the fine wire electrodes, a mechanism that allows rotational and linear movement is required. If designed correctly, electro-mechanical linear actuators can induce linear motion while simultaneously providing position feedback along the rotating axis. To induce rotational movement, a mechanical assembly (Spool Carriage) can be added to the linear actuator. The assembly can provide structural support for a motor, bearings, and the spool as the electrode wire is in the process of being coated. The rate at which the carriage assembly travels must be controllable and determines the amount of wire that gets spun onto the spool with each rotation.

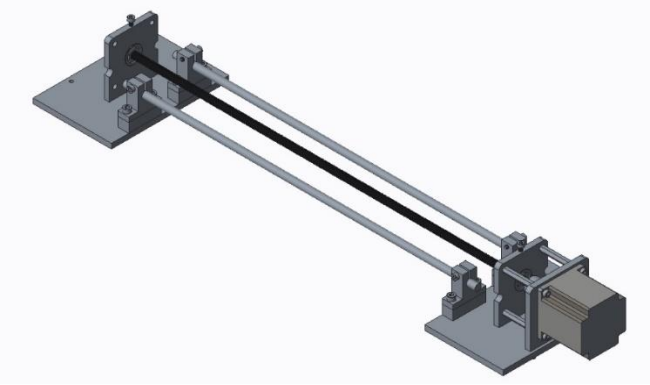

Figure 11. Isometric view of the linear actuator featuring adjustable rail guides and the NEMA 23 stepper motor.

The linear actuator was designed using 6061-T6 Aluminum (McMaster Car), an 8mm diameter lead screw (OpenBuilds Partstore) with 8mm pitch, NEMA 23 High Torque series bipolar stepper motor (OpenBuilds Partstore), an 8mm to 5mm flexible aluminum coupling (OpenBuilds Partstore), case hardened rails (Folger Tech), rail guides (Folger Tech), female hex standoffs (McMaster Car), bearings (McMaster Car), and hex screws (McMaster Car). By using rails guides the width of the assembly can be adjusted to fit into a fume hood, allowing for safe operation. Furthermore, the design is modular. **Figure 11** is a depiction of the linear actuator with a lead screw that was designed and fabricated. The NEMA 23 stepper motor requires a 12-24 VDC source and requires 3 A peak per phase. The step angle is listed at 1.8°± 5% and when coupled with an 8 mm pitch lead screw, permits finely controlled stepping intervals that travel a minimum of 40 μm. Depending on the mother driver that is used, enabling micro-stepping can reduce the travel distance per step, allowing for finer control over the unspooling of the wire.

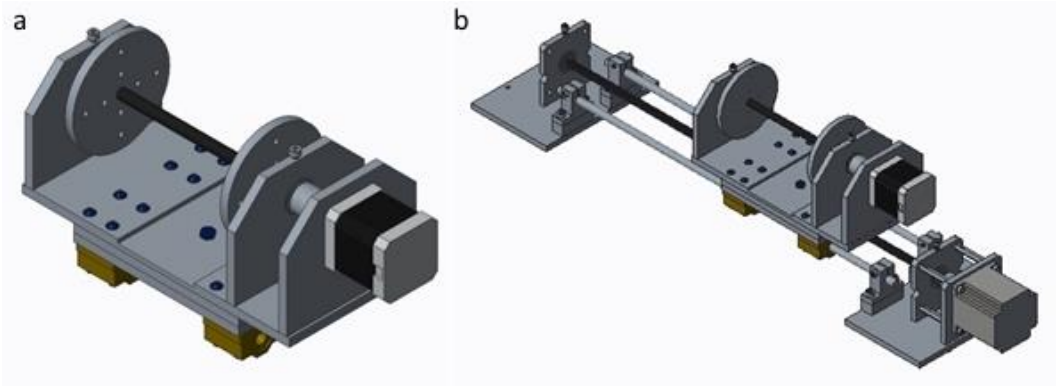

Figure 12. (a) Isometric view of the spool carriage that was implemented onto the linear actuator. (b) The location and placement of the carriage on the linear actuator assembly.

5.4. Spool Carriage

The mechanical assembly that was integrated to the linear actuator is depicted in **Fig. 12**. A fully loaded spool requires 2.71 $\mathrm{N \cdot mm}$ of torque to commence rotation. DC motors can provide sufficient torque but at a higher purchasing cost, therefore a stepper motor is a cheaper alternative to produce the same amount of torque. The spool carriage features a NEMA 17 bipolar stepper motor that permits spooling of the electrode wire. The limitations of using a stepper motor in a continuous coating process are reduced RPM speeds and intermittent stepping intervals at low RPMs, resulting in inconsistent unspooling. To prevent binding of the lead screw during operation of the NEMA 23 stepper motor, an anti-backlash nut block (Openbuilds Partstore) was integrated to the design of the carriage.

5.5. Motor Drivers

The NEMA 17 stepper motors that were integrated into the design of the spool mechanism are rated for 12-24 VDC, 1.5 A, and are two phase bipolar stepper motors. The NEMA 23 stepper motors that have been selected are rated to operate at 12-24 VDC, 3 A, and are two phase bipolar stepper motors. These criteria are essential when selecting a motor driver. The Toshiba TB6560 motor driver proved to be capable of driving the stepper motors without

overheating. The TB6560 can drive stepper motors that operate at 36 VDC and 3 A. It offers adjustability of the running current, the stop current, the excitation modes, and the decay setting. By reducing the excitation modes to 1/16 of a step, the distance the motor steps in response to a pulse is reduced by a factor of 1/16.

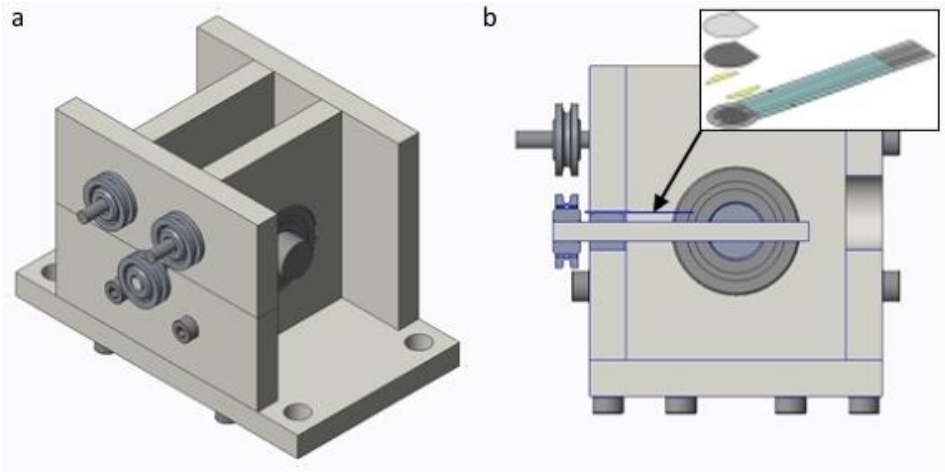

Figure 13. (a) Isometric view of the tension sensor with two static pulleys and a pivoting center pulley. (b) Section veiw of the tension sensor showing the location of the FSR load cell (onset).

5.6. Tension Sensor

To prevent the fine wire electrode from breaking due to the tension produced by the spooling motors, a tension sensor can be designed or purchased, and added in sequence to the coating process (**Fig. 13**). Commercially available wire tension sensors are typically very expensive devices. To ensure the economic efficiency of the assembly, a tension sensor was designed using a polymeric load cell, machinable aluminum (McMaster Car), round stock, bearings, and fine wire pulleys. Interlink Electronics 400 series Force Sensing Resistor (FSR) features a force sensitive range of 0.2 N to 20 N, is mechanically flexible, and withstands 10 million actuations under tapping mode criteria. The design of the tension sensor is based on permitting the center pulley to pivot on bearings and rotate based on the amount of tension in the wire.

5.7. Control System

Using the Arduino as a +5 V power supply and the Arduino analog inputs, the FSR can be integrated into the coating system using the wire schematic depicted in **Fig. 14**. Pinning the FSR between the top faceplate and a custom pressure cube ensures that a force is only applied on the active area of the FSR. The pressure cube is designed to transfer the force from the pivoting center pulley to the FSR. Furthermore, the pressure cube features a small tapered extrusion that is smaller in diameter than the active area of the FSR. The sensitivity of the FSR can be adjusted by increasing the pulldown resistor value (Fig. 14).

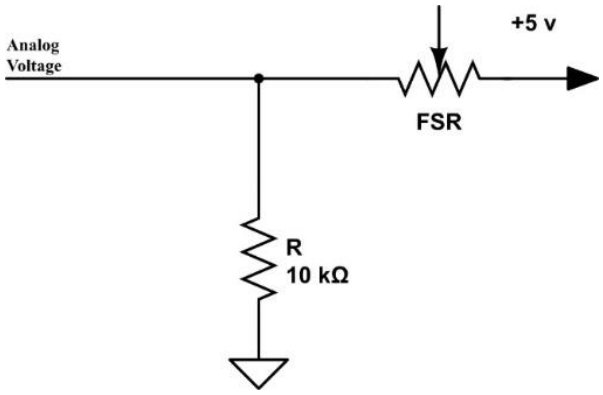

Figure 14. Circuit schematic of the FSR load cell and where R determines the pulldown resistance and increases the sensitivity of the load cell

5.8. FSR Calibration

To initiate the coating process, the wire tension sensor needs to be calibrated to operate within a desired scope. A simple mass balance experiment was conducted to determine the calibration curve. The string was fixed to nut and routed along the pulleys on the tension sensor. A 50 g weight rack was tied to the end of the string and would hang freely off the edge of the counter.

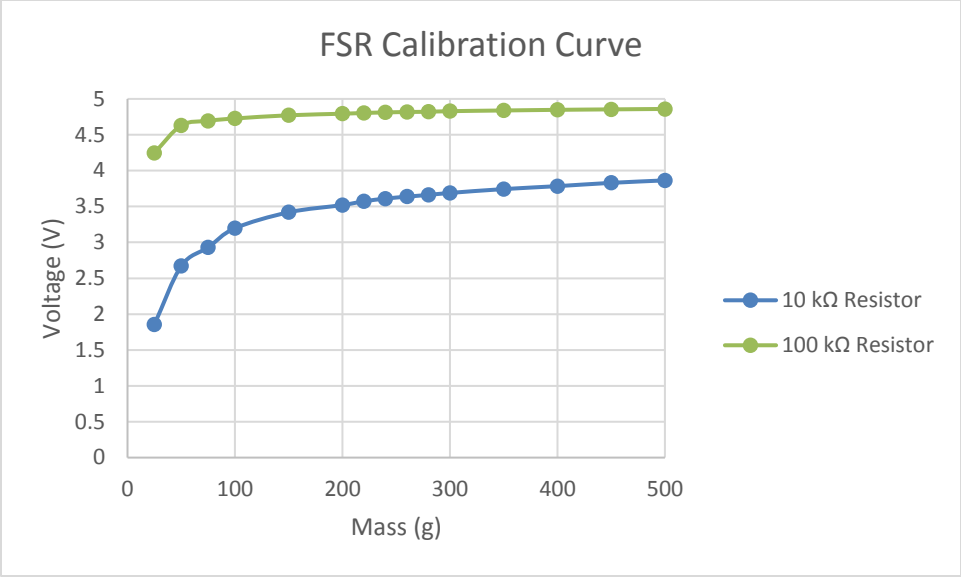

Figure 15. FSR Calibration Curve using 10 kΩ and 100 kΩ resistor. The 10 kΩ resistor provided the best response due to the large voltage discrepancy at higher mass values

The calibration curve for the FSR tension sensor is depicted in **Fig. 15**. The data collected was compared with the product specification and determined to fall within an allowable voltage range. An important note to consider, is that the FSR will warm up after having a load applied for a prolonged amount of time. As the temperature increases, resistance of the FSR decreases, causing the current flowing through the pulldown resistor and the FSR to increase. This will produce voltage measurements that are up to 10% higher. **Eq. 1** is used to determine the voltage and ultimately the load being applied to the wire.

$$V_o = V_s\left(\frac{10k\Omega}{10k\Omega + FSR}\right) \tag{1}$$

Where V_o is the voltage output that is dependent on the FSR resistance, V_s is the voltage supplied to the FSR load cell, and FSR is the varying resistance of the load cell under operation. Analogue pin A2 on the Arduino Mega 2560 is then used to convert the input voltage to an analog value between 0-1023.

5.9. Arduino Sketch

The hardware that permits functionality of the linear actuators, the spool carriage stepper motors, and the tension sensor are controlled using an Arduino Mega 2560. The built-in Arduino stepper motor library enables operation of stepper motors using an appropriate motor driver. However, the Arduino stepper library does not permit two or more motors to run at the same time. If two motors are setup to run independently of each other, Motor A must traverse the number of steps that is commanded by the user before Motor B begins to function. In a dynamic coating process where the carriage spooling motors are required to operate independently and continuously, the Arduino stepper library must be replaced with a custom library. As such, an alternative library was investigated to allow for dynamic and multifunctional control.

5.9.1. Hobby Components Library

An open source custom library that has been shown to work with the Arduino Uno has been developed by Hobby Components. The Hobby Components Library (HCL) was designed to work with DC and stepper motors using a Toshiba TB6560 stepper motor driver. With minor modifications, the library can be programmed to work with an Arduino Mega 2560. Functionalities that were integrated into the HCL added features such as step counting for a continuously operating stepper motor that is being operated by Pulse Width Modulation (PWM) and a method to gauge that the driver RPM matches the command being sent by the Arduino sketch.

The Arduino sketch titled SOL7 was developed to enable functionality of the coating process and is provided in the Supplementary Appendix. SOL7 is intended to be used with four stepper or DC motors. More motors can be added by adjusting parameters in the HCL.

Switching between a stepper or DC motor may require selecting an alternative motor driver. The HCL works in combination with SOL7 to determine the RPM of the motors. The HCL requires a user input time that establishes the stepper motor clock frequency. For a user input time, the frequency is calculated using **Eq. 2**.

$$F = \frac{1}{T \times 100 \times 10^{-6} s} \tag{2}$$

Where F is the frequency of the stepper motor clock in s^{-1} and T is the input time in µs. The frequency can also be used to determine the duration of the duty cycle of the PWM of the signal being sent to the stepper motors. The RPM of the stepper motors can be determined using **Eq. 3**.

$$RPM = \frac{60 \frac{s}{min}}{T \times 200 \frac{steps}{rev} \times 100 \times 10^{-6} s} \tag{3}$$

Where RPM is the revolutions the stepper motor complete in a minute, T is a user input parameter that determines the frequency, and $200 \frac{steps}{rev}$ is calculated by dividing 360° by the travel distance per step 1.8°.

5.9.2. Power State

The power state is designed to default to an off-state upon actuation of the pushbutton. To safely operate a system with a linear actuator that can bind and cause tension at the end points requires the use of single pull dual throw (SPDT) switches. Four switches have been mounted to the rail guides and have been programmed to execute a reverse direction command upon actuation. Alternatively, the position of the carriage can be determined by counting the

numbers of steps the stepper motor has executed. To determine the distance each step will traverse, **Eq. 4** is utilized:

$$\left(\frac{1\text{rev}}{360^\circ}\times\frac{1.8^\circ}{\text{step}}\times\frac{0.008\text{m}}{1\text{rev}}\right)\text{x} = 40\text{x}\,\frac{\mu\text{m}}{\text{step}} \tag{4}$$

Where x is the number of steps that the motor has completed. The line of code that was added to the HCL enables the functionality of counting the number of steps.

5.9.3. Tare State

The tare state aligns the carriage towards a specific location along the lead screw. The state is designed to work with the direction state to select the SPDT that is being actuated. Both carriages travel in the same direction and are triggered to stop according to the SPDT that is triggered. By creating a reference location where the carriage location will be zero along the lead screw, multiple operations can be executed by other states.

5.9.4. Direction State

The direction state was added to orient the carriage towards a rail guide that has an SPDT switch mounted on the top surface. Much like a tare button on a mass scale, the direction state is important to the operation of the mechanism because a rail guide and SPDT is used to generate a reference location where the position along the x-axis is zero.

5.9.5. Run State

The run state has been developed to function with the FSR sensor and provides feedback control of the carriage stepper motors during the coating process. The SPDT switches are active as the NEMA 17 carriage stepper motors progressively unwinds and winds wire from the spools and the larger NEMA 23 stepper motors move the carriage. To provide feedback control of the NEMA 17 stepper motors, additional parameters must be added to increase or decrease the sensitivity at which the FSR sensor requests a speed adjustments to the trailing motor (M2).

A user input FSR voltage setpoint is used to establish a base voltage value (SOL7 line 55). A user adjustable buffer or voltage offset (SOL7 line 56) from the setpoint is used to provide a permittable tension range before an RPM adjustment is requested from SOL7. The increment at which the RPM is modified must vary according to the RPM value. For example, if the user input RPM value is less than 1, the incremental/decremental value must be less than 0.01. An appropriate RPM response to the tension in the wire is depicted in **Fig. 16**.

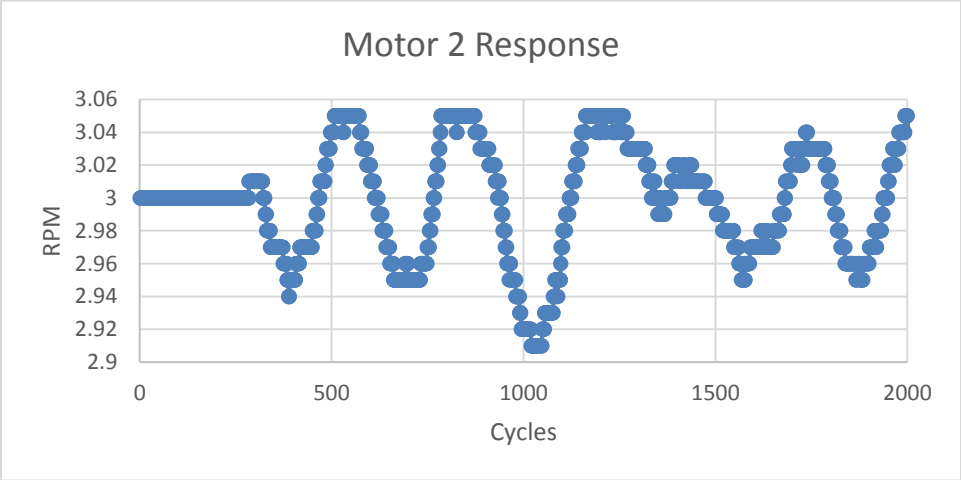

Figure 16. Motor 2 response according to the tension in the SS wire as it progresses through the coating process. Parameters are set at 3 RPM, 3.0 V FSR setpoint and 0.3 V buffer offset before and adjustment is made. The RPM increases/ decreases at 1/100th the user input RPM (±0.01 RPM).

If the decremental value is too large and if Motor 2 is rotating at a speed that is producing low tension in the wire, this will induce the RPM to reach zero after minimal loop iterations. A general rule of thumb can be established that for any given RPM value, the incremental/ decremental operator must be smaller than 1/100th of the input value. As the RPM is increased, the incremental/ decremental operator can be increased to values that are greater than 0.01. A maximum allowable RPM has been added to the code and prevents the wire from spontaneously losing tension. If the alignment of the wire along the spool is off center from the wire tension sensor, the wire has the tendency to adjust and move to point on the spool that

only produces a tension force on the wire. This occurs if the wire is wound onto the spool manually or if the wire gets caught on a ridge during the automated winding process. The spools that are used on M2 and M3 contain micro-ridges as a result of the 3D printing process.

Since the Arduino Mega 2560 can measure the RPM rate faster than the stepper motors iterates through a step, a delay parameter has been added to the code that will measure the RPM after SOL7 has iterated a user input amount of times. The HCL has a parameter that permits adjusting the amount of times the library is executed. It is based off the default Arduino clock frequency and is effectively known as an interrupt.

5.9.6. Wire Tension State

The wire tension state was added to the program to apply a tension preload on the electrode wire before the coating process was initiated. This ensured that no slack remained in the wire prior to coating. After multiple trials, it was determined that excessive slack in the wire prevents successful coating of the electrode wire if a syringe coating method is being used. Since the run state is intended to be operated after the wire tension state is complete, the voltage setpoint is the same input as the run state (SOL7 line 55). The rate at which Motor 3 has been programmed to rotate is a constant 0.5 RPM. Motor 2 is fix at zero rotation until the user input tension value is detected by SOL7. At this point, the program leaves the wire tension state and is ready to execute any other state.

5.10. Electrical Components

All wire gauges have been selected to correspond with the amount of rated current required to operate the machinery. The NEMA 23 stepper motor requires 3 A driving current and using the American wire gauge (AWG) standards for a bundled conductor (0.8 correction factor), Polyvinyl Chloride (PVC) coated 18 AWG wire (Remington Industry, 4.9 A) can safely handle

3.92 A. The NEMA 17 stepper motors require 1.5 A to operate and using the same calculation, PVC coated 22 AWG wire (Remington Industry, 2.1 A) can safely handle 1.68 A. All wires have been crimped to appropriately sized plugs and receptacles to facilitate power transfer and the assembly of the machinery. All the wires have been wrapped in ¼" Polyethylene Terephthalate expandable braided sleeves (Electriduct). Connections to switches which are intended to be used permanently have been soldered using silver solder. A printed circuit board will be designed to replace the breadboard in later iterations of the device. 12 V and 24 V power supplies (Mean Well) were selected to power the stepper motors and are CSA certified.

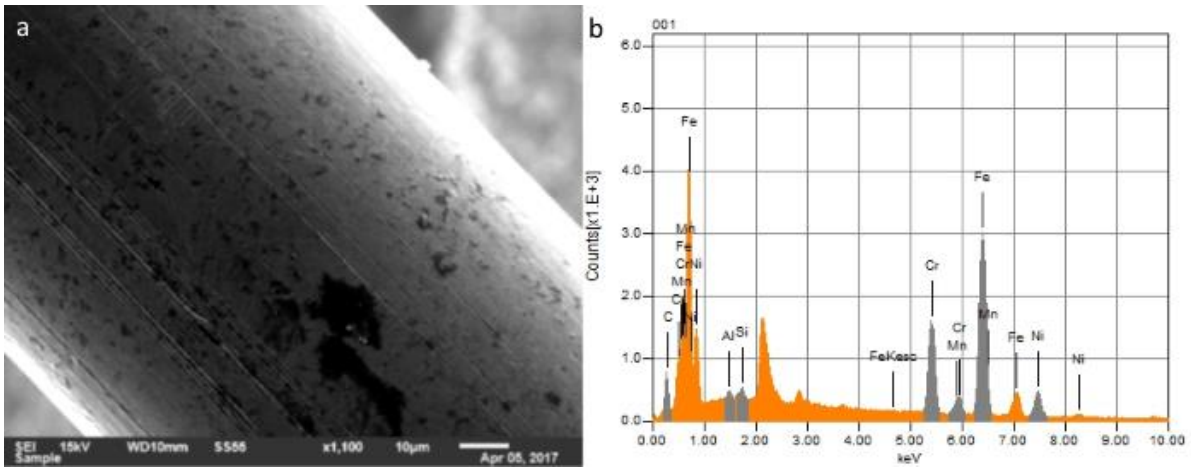

Figure 17. (a) SEM of 101.6 µm 316 LVM SS wire from the supplier and (b) the EDS spectra.

6. Discussion

Multiple characterization methods were used to determine successful film deposition, the corresponding film composition, and the surface features of each layer. Using SEM, the as delivered SS wire was characterized. EDS was used as an elemental analysis tool of the SS wire composition. **Figure 17a** shows an SEM image of the 101.6 µm SS wire, while Fig. 17b is the EDS spectra of the reference wire. Comparing the EDS results with the raw materials

characteristic data that was supplied by the wire manufacturer, the lack of a prominent Molybdenum peak has been noted, and is attributed to use of a K-α electron source.

AFM was used to determine the surface roughness of the reference wire. **Figure 18a** shows the surface roughness of the reference wire, where the root mean square (RMS) surface roughness was determined to be 3.14 ± 1 nm. Different areas of the wire were sampled as a process to determine the effects of conducting AFM on a curved surface, and to ensure that the sampling was done near the apex of the wire.

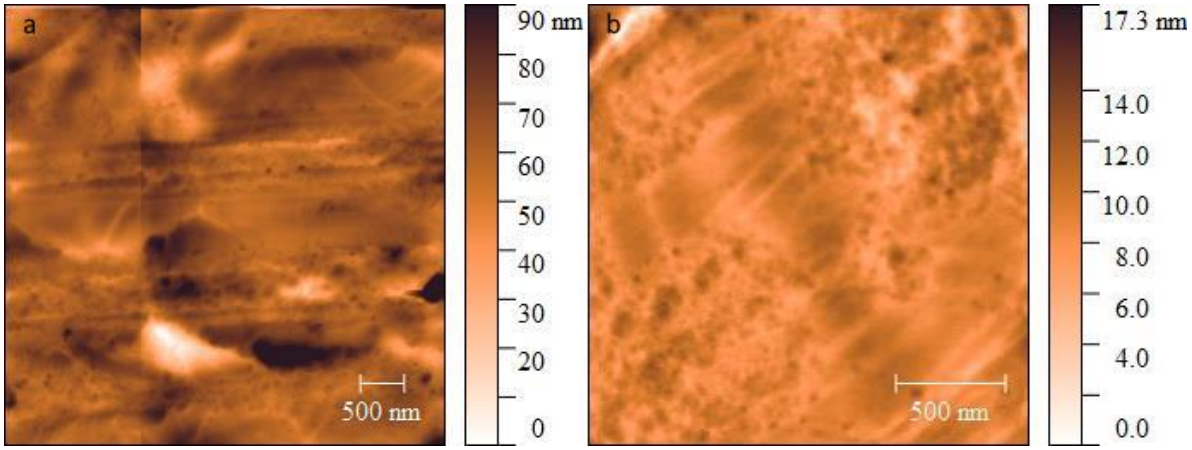

Figure 18. (a) Topography of the SS wire with an RMS surface roughness of 3.14 nm and (b) AFM of the TiO_x coat that was deposited using a 20% by volume solution of Titanium (IV) butoxide at 3 RPM.

With the RMS of the reference wire known, a solution of 20% by volume of Titanium (IV) butoxide was mixed with isopropyl alcohol. The wires were coated at a rate of 1, 3, and 10 RPM (36.9 cm/min – 1.2 m/min) and dried for 156 s, 52 s and 15.6 s respectively, at 120 °C. Drying at 120 °C produces amorphous TiO_x and there has been sufficient evidence to prove that the properties of amorphous TiO_x will remain the same, regardless of if they have been deposited in ambient conditions or in a glovebox.[21] Since the PSC fiber is intended to be manufactured in ambient conditions with few methods of controlling contamination, the

importance of successfully processing a layer of TiO_x in ambient conditions is considered a highlight of the inline dip coating process. **Figure 19a** shows an SEM image of a wire that has successfully been coated at 3 RPM to form a layer of TiO_x. Using AFM, the RMS surface roughness was determined to be 1.46 ± 1 nm. EDS confirmed the presence of TiO_x (Fig. 18b).

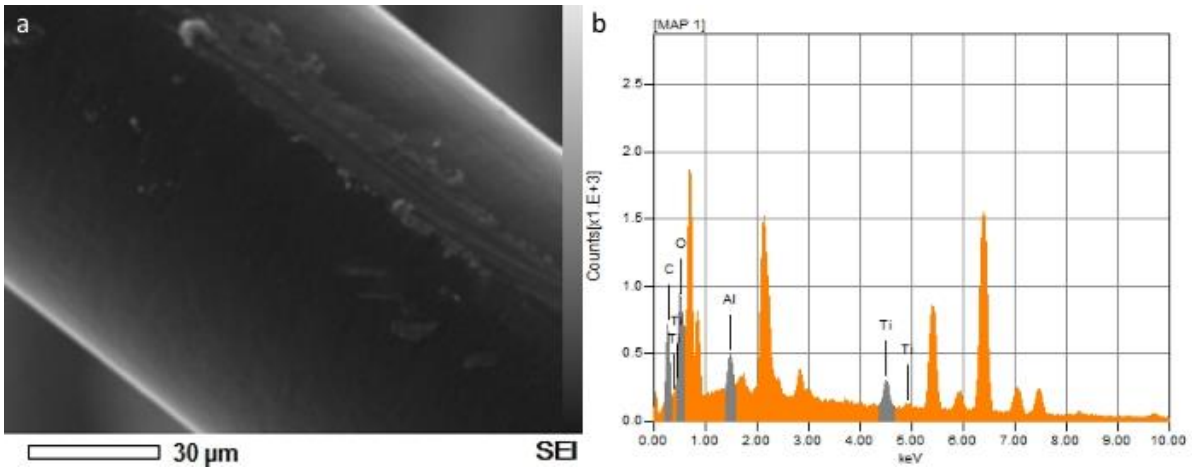

Figure 19. (a) SEM electrode wire that has successfully coated with TiO_x and (b) the EDS spectra indicated the presence of titanium and oxygen in the material.

Determining the thickness of the coating that has been deposited has proven to be a challenge. One method of determining the coat thickness was by use of profilometry. Since the height of a coated wire can be measured from the apex and the diameter of the electrode wire is known, the difference between the measured value and the diameter would provide the film thickness. A reference SS wire sample and two samples that had been coated with TiO_x at speeds of 1 and 10 RPM were measured. The samples were placed on glass and two pieces of tape was placed over the wire, leaving a 2 cm spacing where the wire was exposed. By placing the tape over the wire, ensured that any defects in the tape would not be included in the overall height measurement of the samples. The spacing between the pieces of tape produced a flat zero reference line followed by a smooth parabolic profile as the tip of the profilometer was probing the surface. The location and the angle at which the probe approached the wire was

varied for each measurement of a sample. It was discovered that the wire was mechanically deforming as the speed of the coating process was increased. A plot of the data that was collected is depicted in **Fig. 20.**

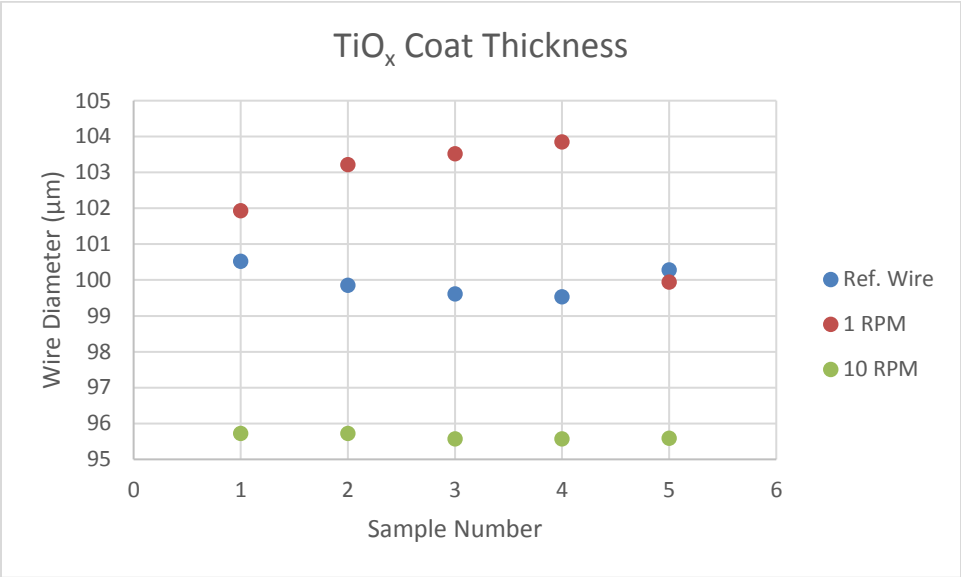

Figure 20. Profilometry results to determine the thickness of the wire. The reference wire is within an acceptable tolerance range. The 1 RPM points are indicating that TiO_x has been coated on the wire. The 10 RPM points are indicating that the wire has been plastically deformed at higher speeds.

The Certificate of Compliance issued by the manufacturer of the 101.6 µm electrode stated that the yield strength of the material is 501 MPa. The 101.6 µm SS electrode will yield under an applied load of 436 g (4.27 N) and will fail at 634 g (6.21 N) at which point the wire will have elongated 43%. A request for clarification from the company lead to the discovery that the yield strength widely varies from 379-689 MPa. While attempting to coat the TiO_x at 20 RPM, the wire failed under a tensile stress of 342 MPa. A hypothesis to explain the premature failure is based on an observation that the failure occurred within the span of the wire that was passing through the oven. Previous literature suggests that for samples of carbon based steels, the softening effect on the material's tensile strength should only be 5% of the yield strength

at 150 °C.[22,23] **Figure 21** is a direct comparison between the factor of safety using two different yield strengths that have been temperature adjusted. The factor of safety can be determined using **Eq. 5.**

$$n = \frac{\sigma_{Y.S.}}{\sigma_T} \tag{5}$$

Where n is the factor of safety of the wire as the machine is being operated, $\sigma_{Y.S.}$ is the yield stress of SS electrode, and σ_T is the calculated tensile stress on the material.

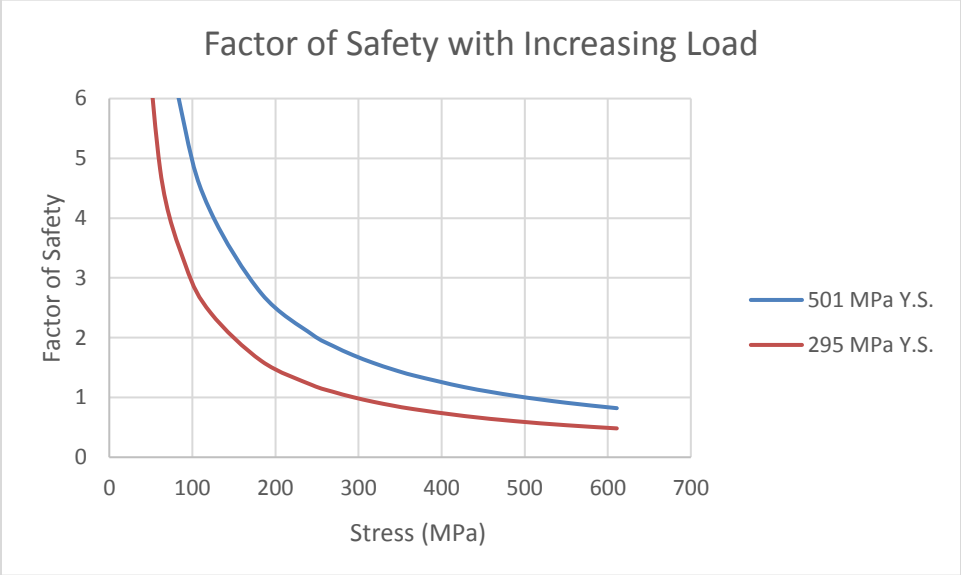

Figure 21. The factor of safety with increasing tension in the wire using a corrected yield strength of 501 MPa (derived from the Certificate of Compliance) and 295 MPa using the manufacturers advertised yield strength value.

From the trendline that is observed, the wire is expected to fail under an applied stress of 342 MPa if the yield strength that is published by the manufacturers website is used in lieu of the yield stress indicated in the Certificate of Compliance. Furthermore, this explains why the wire is deforming at high speeds. If the voltage setpoint for the FSR was set at an acceptable level and if the voltage offset for permissible tension in the wire was too large, the system would not be able to respond quick enough to reduce the tension in the wire.

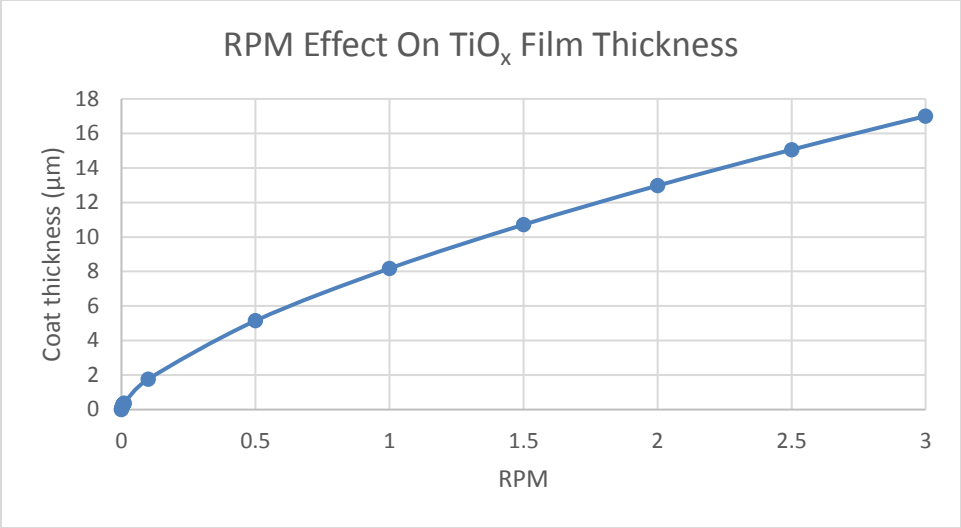

Figure 22. Theoretical effect on 20% by volume of TiO_x film thickness when the RPM is increased.

Dip coating has long been used as a method to coat thin films on substrates such as electrodes, optical fibers, and wires. By treating the syringe coating method as a modified horizontal dip coating process, the Landau-Levich equation (**Eq. 6**) can be used to estimate the approximate film thickness that will be coating onto the SS electrode.[24,25]

$$h = 0.94\frac{(\eta \times \nu)^{2/3}}{\gamma^{1/6}(\rho \times g)^{1/2}} \tag{6}$$

Where h is the thickness of the thin film, η is the viscosity (4.5 cP), ν is the withdrawal speed, γ is the liquid-vapor surface tension ($0.028\,N \cdot m^{-2}$), ρ is the density ($828.8\,kg \cdot m^{-3}$), and g is the gravitational acceleration. By measuring the thickness of the TiO_x at different RPM, it can be determined whether the Landau-Levich equation holds true for the syringe coating method. A general trendline that should be observed is depicted in **Fig. 22**. The Landau-Levich theory states that as the velocity of the substrate being submersed is increased, the coat thickness will increase. The Landau-Levich equation does not take into consideration

the evaporation of the solvent and will require a correction factor that will be empirically determined based off the samples that have been coated. The thickness of a film can be reduced by decreasing the viscosity of the solution. This can be accomplished by heating the solution before initiating the coating process.

7. Conclusion

The machinery that was designed is capable of continuously coating SS wire electrodes with precursor solutions at up to speeds of 1.2 m/min. Low annealing temperatures can be used and the morphology of the layers can be adjusted by increasing or decreasing the time in the oven. The tension sensor that was designed is capable of actively calculating the tension in the wire during any given iteration. The syringe coater and the pump can recirculate the solutions that were prepared, effectively reducing the overall volume of material that is necessary to process a layer. The pump can hold steady state of flow using a minimum of 4 mL of prepared solution. The machine has successfully been operated for 12 minutes where a layer of TiO_x was successfully deposited.

Some minor adjustments are needed to ensure that the machine is consistently producing the same results during varying tests. The current oven design does not permit annealing the processed layers for the same time at different speeds. If the Landau-Levich equation is determined to effectively calculate the thickness of the layer that is to be expected, a modification is necessary to the syringe coater that will ensure decreased thin-film thickness at higher speeds. The FSR sensor failed prematurely and required a new calibration when the replacement was installed. The wire failed when a low stress was exerted on the wire. Furthermore, the deformation that is present in the wires after processing is concerning.

8. Future work

The current feedback logic that is implemented to run the coating process is based on controlling two stepper motors. By eliminating the NEMA 17 stepper motors that are on the spool carriage and replacing them with NEMA 17 DC motors, the built-in Arduino PID library can be implemented. Furthermore, since DC motors work in a continuous manner, the intermittent delays that are typical in stepper motors would no longer cause a periodic increase in tension. The TB6560 motor driver, the NEMA motor interface, and the HCL have been selected specifically to permit change in motor controls without the need for retrofitting.

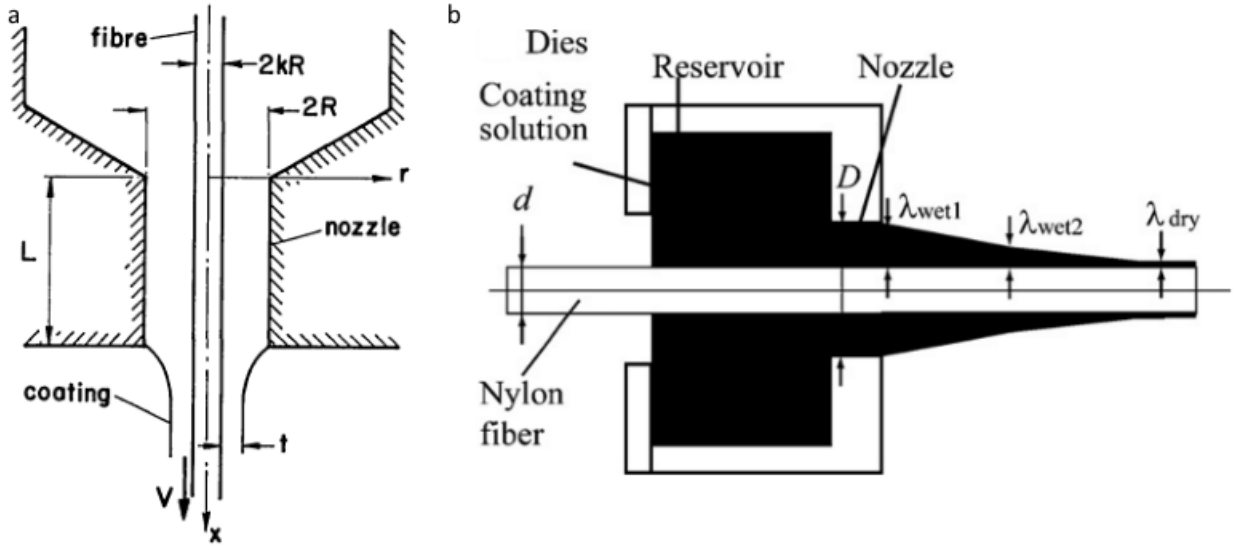

Figure 23. (a) Schematic of a cup coater depicting the fiber coating flow and (b) modified horizontal cup coater design containing a reservoir for the solution and a nozzle. Reproduced with permission from [26,27].

In Konarka Technologies original patent, the use of a cup coater ensured that the thin film that was deposited remained within an acceptable thickness (**Fig. 23a**). The geometry of a cup coater follows the design of a nozzle with an orifice diameter 2R and a die with an orifice length L. Most importantly, as a wire of diameter 2kR is pulled through the orifice at low speeds with laminar fluid flow, the thickness coated on the wire becomes dependent on the

geometry of the cup coater.[26] The viscosity and the surface tension of the fluid can be neglected. Furthermore, the effects of surface tension in a cup coater are minimal at high drawing velocities or with the addition of a pressurized cup coater. A correctly designed cup coater permits the coating of a fiber at high velocities where the layer thickness has no dependence on velocity and surface tension, which two important variables in the Landau-Levich equation (Eq. 5). This was proven during the coating process of nylon fibers with PEDOT:PSS that were to be used as pressure sensors.[27] If the speed of the wire can be increased or decreased without having effect on the thickness of the film that is deposited, and if the oven is retrofitted to adjust lengths with changing motor speed, the annealing time for each layer can be held constant.

While the FSR load cell can determine changes in the tension of the wire as it progresses through the coating process, the variation in resistance as the temperature increases is concerning. Coupled with the fact that the load cell failed prematurely within four months of testing, there is clearly a need for selection of a different type of load cell. A Honeywell FSG15N1A load cell is a piezoelectric silicon load sensing element that requires amplification and does not suffer from a large sensitivity shift as the operating temperature increases. Changing the load cell will require minor changes to the design of the tension sensor assembly but it can easily be integrated to SOL7 by using an HX711 load cell amplifier.

Lastly, the wire needs to be tensile tested to determine if the yield strength stated on the certificate of compliance is valid. Furthermore, it is necessary to establish a temperature correction factor to determine the effect of annealing on the wire at relatively low temperatures.

Acknowledgments

The author would like to thank Professor Luscombe for the opportunity to conduct research in her lab group. The author would like to thank Dr. Sarah Holliday, Wesley Tatum, and Jonathan Onorato for their assistance, advice, and editing this paper. The author acknowledges the team effort of undergraduates Wyatt Homola, Parker Newman, and Luocheng Huang to complete this project. With kind regards, the author acknowledges financial support from the Hispanic Scholarship Fund and The Coca-Cola Company. Part of this work was conducted at the Molecular Analysis Facility, which is supported in part by funds from the Molecular Engineering & Sciences Institute, the Clean Energy Institute, the National Science Foundation, and the National Institutes of Health.

References

[1] H. Shirakawa, E. J. Louis, A. G. MacDiarmid, C. K. Chiang, A. J. Heeger, *J. Chem. Soc., Chem. Commun*. **1977**, 578.

[2] C. J. Brabec, J. R., Durrant. *MRS Bulletin*. **2008**, 33, 670.

[3] S. Günes, H. Neugebauer, N. S. Sariciftci, *Chemical Rev.* **2007**, 107, 1324.

[4] G. Yu, A. J. Heeger, *Journal of Applied Physics.* **1995**, 78, 4510.

[5] J. Zhao, Y. Li, G. Yang, K. Jiang, H. Lin, H. Ade, H. Yan, H. *Nature Energy*. **2016**, 1, 15027.

[6] S. Venkatesan, J. Chen, E. C. Ngo, A. Dubey, D. Khatiwada, C. Zhang, Q. Qiao, *Nano Energy*. **2015**, 12, 457.

[7] L. Chang, H. W. Lademann, J. B. Bonekamp, K. Meerholz, A. J. Moulé, *Advanced Functional Materials*. **2011**, 21, 1779.

[8] A. Dubey, P. Saini, Q, Qiao, in *Fundamentals of Conjugated Polymer Blends, Copolymers and Composites: Synthesis, Properties, and Applications*. (Eds: P. Saini), John Wiley & Sons, Canada **2015**, Ch. 5.

[9] R. Po, C. Carbonera, A. Bernardi, N. Camaioni, *Energy & Environmental Science*. **2011**, 4, 285.

[10] M. T. Greiner, Z. H. Lu, *NPG Asia Materials*. **2013**, 5, e55.

[11] J. Onorato, V. Pakhnyuk, C. K, Luscombe. *Polymer Journal*. **2017**, 49, 41.

[12] R. R. Søndergaard, M. Hösel, F. C. Krebs, *Journal of Polymer Science Part B: Polymer Physics*. **2013**, 51, 16.

[13] X. Gu, Y. Zhou, K. Gu, T. Kurosawa, Y. Guo, Y. Li, C. J. Tassone, *Advanced Energy Materials*. **2017**.

[14] M. R. Lee, R. D. Eckert, K. Forberich, G. Dennler, C. J. Brabec, R. A. Gaudiana, *Science.* **2009,** 232.

[15] T. Chen, L. Qiu, Z. Yang, H. Peng, *Chem. Soc. Rev*. **2013**, 42, 5031.

[16] S. Lee, Y. Lee, J. Park, D. Choi, *Nano Energy*. **2014**, 9, 88.

[17] Z. Zhang, Z. Yang, Z. Wu, G. Guan, S. Pan, Y. Zhang, H. Peng, *Advanced Energy Materials*. **2014**, 4, 1301750.

[18] Z. Zhang, X. Chen, P. Chen, G. Guan, L. Qiu, H. Lin, H. Peng, *Advanced Materials*. **2014** 26, 466.

[19] D. Liu, Y. Li, S. Zhao, A. Cao, C. Zhang, Z. Liu, C. Huang, *RSC Advances*. **2013**, 3, 13720.

[20] T. Kobayashi, M. Bando, N. Kimura, K. Shimizu, K. Kadono, N. Umezu, Y. Murakami, *Appl. Phys. Lett.* **2013**, 102, 023112.

[21] S. Lattante, *Electronics*. **2014**, 3, 132.

[22] E.A. Brandes, in *Smithells metals reference book*, Butterworth Publishers, Stoneham, Massachusetts **1993**, Ch. 22.

[23] J. E. Shigley, C. R. Mischke, R. G. Budynas, in *Mechanical Engineering Design*. McGraw-Hill, **2004**, Ch. 1.

[24] N. Barati, M. F. Sani, H. Ghasemi, Z. Sadeghian, S. M. Mirhoseini, *Applied Surface Science*. **2009,** 255, 8328.

[25] D. Quéré, *Annu. Rev. Fluid Mech*. **1999**, 31, 347.

[26] A. Panoliaskos, W. L. Hallett, I. Garis, *Applied optics*. **1985**, 24, 2309.

[27] S. Takamatsu, T. Kobayashi, N. Shibayama, K. Miyake, T. Itoh, *Sensors and Actuators A: Physical*. **2015**, 184, 57.